SCIENCE CHINA
Information Sciences

• RESEARCH PAPER •

October 2017, Vol. 60 102305:1–102305:17
doi: 10.1007/s11432-016-9017-6

Compressed sensing application in interferometric synthetic aperture radar

Liechen LI[1,2*], Daojing LI[1,2] & Zhouhao PAN[1,2]

[1]*Science and Technology on Microwave Imaging Laboratory, Beijing* 100190*, China;*
[2]*Institute of Electronics, Chinese Academy of Sciences, Beijing* 100190*, China*

Received July 9, 2016; accepted January 21, 2017; published online June 22, 2017

Abstract A novel interferometric synthetic aperture radar (InSAR) signal processing method based on compressed sensing (CS) theory is investigated in this paper. InSAR image formation provides the scene reflectivity estimation along azimuth and range coordinates with the height information. While surveying the height information of the illuminated scene, the data volume enlarges. CS theory allows sparse sampling during the data acquisition, which can reduce the data volume and release the pressure on the record devices. InSAR system which configures two antennas to cancel the common backscatter random phase in each resolution element implies the sparse nature of the complex-valued InSAR image. The complex-valued image after conjugate multiplication that only a phase term proportional to the differential path delay is left becomes sparse in the transform domain. Sparse sampling such as M-sequence can be implemented during the data acquisition. CS theory can be introduced to the processing due to the sparsity and a link between raw data and interferometric complex-valued image can be built. By solving the CS inverse problem, the magnitude image and interferometric phase are generated at the same time. Results on both the simulated data and real data are presented. In comparison with the conventional SAR interferometry processing results, CS-based method shows the ability to keep the imaging quality with less data acquisition.

Keywords synthetic aperture radar (SAR), interferometric synthetic aperture radar (InSAR), compressed sensing (CS), sparse sampling, sparsity in the transform domain

Citation Li L C, Li D J, Pan Z H. Compressed sensing application in interferometric synthetic aperture radar. Sci China Inf Sci, 2017, 60(10): 102305, doi: 10.1007/s11432-016-9017-6

1 Introduction

Interferometric synthetic aperture radar (InSAR) has been developed since 1970s and is a technique extensively used to extract the information from the phase of the SAR signal [1, 2]. InSAR systems take advantage of the two or more antennas by exploiting the phase information. This additional phase information can be used to obtain height information of the illuminated scene, measure the radial velocity of moving scatterers, or monitor surface deformation depending on the implementation [3, 4]. In this paper, we focus on cross-track interferometry, although the proposed ideas may extend to the other modes of interferometry. However, with more information acquired, much more data are needed during the acquisition and processing. While the volume of data collected is increasing rapidly, the ability to

* Corresponding author (email: lilc311@163.com)

transmit it, or to store it, is not increasing as fast. As a result, an effective data acquisition approach such as sparse sampling is necessary.

Conventional InSAR data acquisition must obey the Nyquist Sampling Theorem. If non-uniform sampling is implemented during the data acquisition, imaging results will deteriorate rapidly due to the high sidelobe and grating lobe. Compressed sensing (CS), as a favorable sparse reconstruction technique, is a new and attractive method for sparse sampled data imaging and has attracted many attention [5,6]. CS indicates that certain signals can be recovered with far fewer samples or measurements than traditional method.

Inspired by the idea of CS, more and more novel processing methods in radar imaging have been proposed. For example, ref. [7] introduced CS into radar imaging which aims at eliminating the need for the pulse compression matched filter at the receiver, and reducing the required receiver bandwidth. High resolution ISAR imaging method during short coherent interval was presented in [8]. Ref. [9] applied CS on multi-baseline InSAR data for layover separation and analyzed the effect of signal-to-noise ratio (SNR) and height difference of CS based method. Refs. [10–12] studied SAR tomography and three-dimensional imaging using CS. Some applications of CS in SAR imaging are also concerned about recently [13–15]. Among these studies, many researchers used CS to reconstruct high resolution image of sparse targets, such as ships, aerial targets and persistent scatterers along elevation directions. However, in practical cases, many scenes are not sparse such as the forest area. Furthermore, compared with optical images, complex-valued SAR images exhibit significantly higher dynamic range and less spatial correlation due to the random phase of each resolution element [16]. Thus, common sparse representation to optical images is not suitable for the complex-valued SAR images. A SAR image obtained by single aperture can hardly be sparsely represented. It becomes a key challenge for InSAR images to choose the right representation scheme.

To find an appropriate scheme other than the identity matrix, researchers developed many new approaches. Cetin et al. [17,18] established a series of work focusing on sparsely representing the magnitude image in the transform domain, which enlightens a method that separates the complex-valued image into two parts for processing. The work about multi-baseline SAR interferometry also inspired the researchers combining the data from multi-channel in signal processing [19]. In InSAR systems, two antennas bring more information and redundancy than a single one which creates an opportunity for SAR images to be represented sparsely.

In this paper, we propose a new method which surveys the roles of sparsity and CS elements in InSAR imaging. The InSAR systems cancel the common backscatter random phase and use the phase difference of two antennas to derive an altitude for each image point. Since the altitude is continuous and slow-varying, the phase difference proportional to it has the same property, which means the scene can be sparsely represented. The proposed method takes advantage of this point and can reduce the required number of measurements releasing the pressure on the data acquisition part of the InSAR system. The novelty of this paper lies in the idea that representing the complex-valued SAR image in the transform domain by interferometric processing. The proposed method can form an image of scene not sparse in the space using sparse samplings. Both the image magnitude and interferometric phase can be kept with a few samplings.

The remainder of this paper is given as follows. The next section describes the sparsity of InSAR images and a CS formulation of the InSAR imaging problem. The InSAR imaging method based on CS is proposed in Section 3. Section 4 gives extensive experimental results on simulated data and real data along with a performance analysis of the proposed method. Experiments with three-baseline millimeter wave InSAR data were performed, and the results show that the scheme works successfully. Section 5 summarizes the properties of the new method and addresses the future developments.

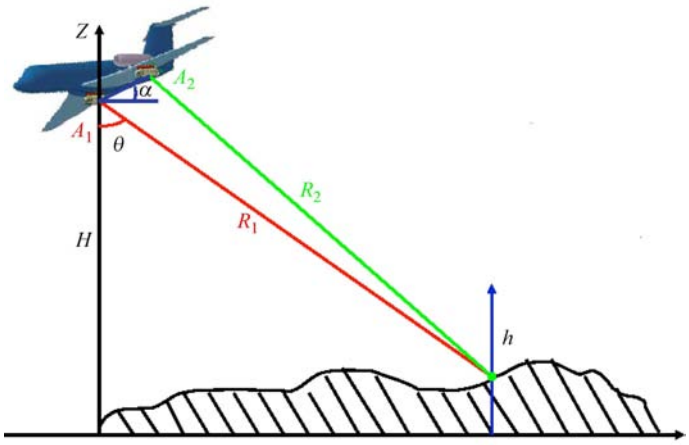

Figure 1 (Color online) InSAR geometry projected on height-ground range plane.

2 Sparsity of InSAR signal

The basic principles of InSAR have been described in detail in many related literatures and the concepts of sparse reconstruction algorithms are central themes in CS and have been presented in many years. Based on these foundations, this section presents a brief survey of these themes while also drawing connections between the InSAR and CS.

2.1 InSAR geometry and sparsity

The sparsity of the InSAR signal is analyzed in this section. Figure 1 illustrates the InSAR system. In a single antenna case, antenna A_1 transmits signals such as chirp signal and receives the echo. By pulse compression technique in range direction and synthetic aperture principle in azimuth resolution, two-dimensional (2-D) high resolution radar images are achieved. For each resolution element of this image, it can be represented as a complex phasor of the propagation phase delay (proportional to the propagation route R_1) and the coherent backscatter from the scattering elements on the ground [20]. Because the resolution element is much greater than the wavelength, a resolution element can be considered as consisting of many individual elemental scatterers within the cell. Hence, the backscatter phase delay can be expressed as the net phase of the coherent sum of the contributions from all elemental scatterers in the resolution element [20],

$$\phi_{\rm b} = \arg\left\{\sum_i A_{\varepsilon i} {\rm e}^{{\rm j}\phi_{\varepsilon i}} {\rm e}^{-{\rm j}\frac{4\pi}{\lambda}R_{\varepsilon i}}\right\}, \tag{1}$$

where $A_{\varepsilon i}{\rm e}^{{\rm j}\phi_{\varepsilon i}}$ is the backscatter of the ith elemental scatterer, $R_{\varepsilon i}$ is its differential path delay and λ is the wavelength.

Typically, 2-D Fourier transform (FT) is used as the representation of the energy of complex-valued images. However, the energy of the coefficients of 2-D FT of the complex-valued SAR image distributes in the whole frequency domain. Due to the impact of the backscatter random phase $\phi_{\rm b}$, a SAR image can hardly be sparsely represented.

In InSAR case, while radar pulses are transmitted from the conventional SAR antenna A_1, radar echoes are received by both the conventional and an additional SAR antenna A_2 shown in Figure 1. The phases of two nearby antennas can be expressed as

$$\begin{cases} \phi_1 = 2\dfrac{2\pi}{\lambda}R_1 + \phi_{\rm b1}, \\ \phi_2 = 2\dfrac{2\pi}{\lambda}R_2 + \phi_{\rm b2}, \end{cases} \tag{2}$$

where R_2 is the distance between Antenna A_2 and the target, $\phi_{{\rm b}i}$ $(i = 1, 2)$ is the antenna A_i's backscatter phase. The basic assumption of InSAR systems is that the backscatter phase delay of each resolution

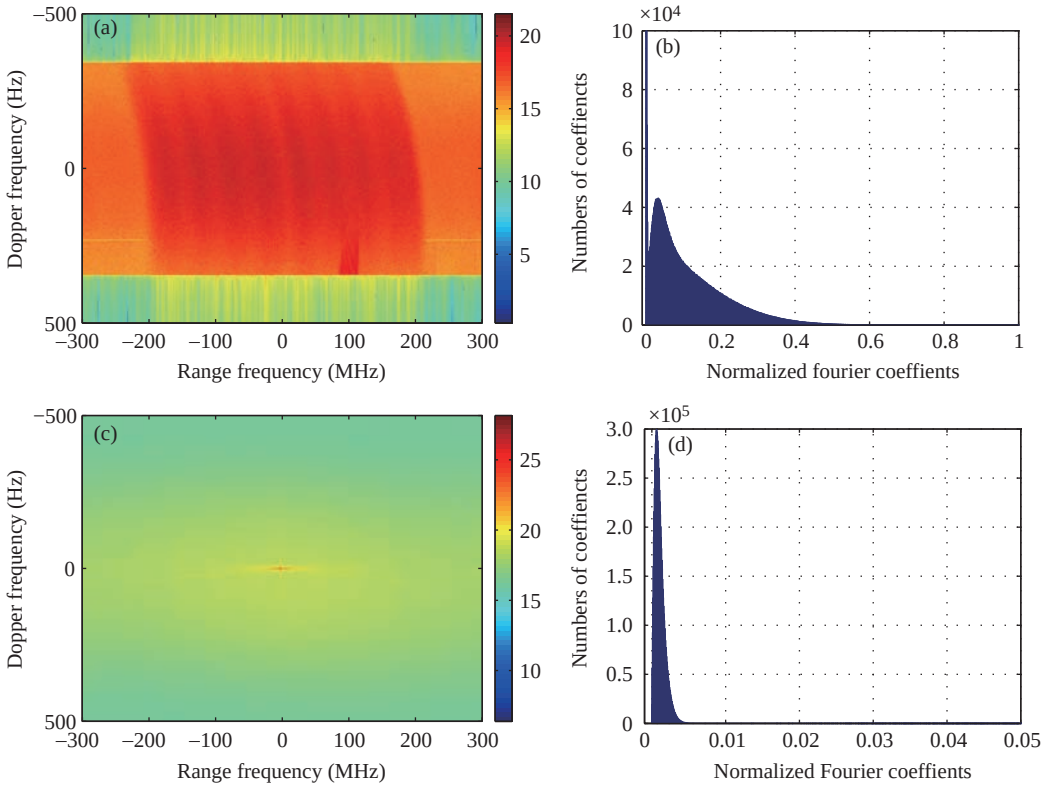

Figure 2 SAR image spectrum. (a) The spectrum before the backscatter random phase cancellation; (b) histogram of the original spectrum; (c) the spectrum after the backscatter random phase cancellation; (d) histogram of the spectrum after the backscatter random phase cancellation.

element keeps unchanged if the view angles of two antenna are nearly the same. The view angles are usually much less than 1° in practice, so the backscatter phase delays are approximately the same, that is, $\phi_{\mathrm{b}1} \approx \phi_{\mathrm{b}2}$.

By coherently combining the signals from the two antennas, the interferometric phase difference between the received signals can be formed for each image pixel. The conjugate multiplication can effectively cancel the common random backscatter phase in each resolution element, but leave a phase term proportional to the differential path delay [20]. Since the nature scene is usually continuous, the differential path delay is also continuous and slow-varying. Taking advantage of this property, we reconstruct the complex-valued image as

$$I_1' = I_1 \exp(-\mathrm{j}\phi_2), \tag{3}$$

where I_1 is the complex image obtained by antenna A_1 and I_1' is the reconstructed image. With this reconstruction, the backscatter random phase delay which contributes to the high frequency part can be reduced.

The real data images shown in the Section 4 display a typical SAR image of an agricultural area acquired by three-baseline millimetre wave InSAR of Institute of Electronics, Chinese Academy of Sciences (IECAS). The magnitude image shows that the scatterers are distributed uniformly in most of the illuminated area. The sparse assumption that the number of targets is much less than the total number of discrete spatial positions investigated by many papers is not satisfied. As we have known, the SAR image phase is noise-like and unsmoothed, which indicates that the complex-valued SAR image may not be sparsely represented in some other transform domains.

Figure 2 shows the spectrum of the SAR image before and after the backscatter random phase cancellation (logarithmic operation is taken here). Figure 2(a) is the original spectrum which the principal frequencies distribute in a wide range, while the spectrum in Figure 2(c) only consists of a few principal frequencies. The histogram of the Figure 2(a) in vector form is shown in Figure 2(b), the Fourier

coefficients mainly distribute in the range $(0, 0.4]$ which indicates poor sparsity. After multiplication by the complex conjugate phasor information of the second image as shown in (3), common backscatter random phase in each resolution element is effectively cancelled, leaving a phase term proportional to the differential path delay which is called "interferogram". Figure 2(d) shows the spectrum histogram of the reconstructed image, the Fourier coefficients mostly concentrate around zero of the normalized frequency, which is highly sparse. The result shown in Figure 2(d) indicates the InSAR image can be sparsely represented in the frequency domain.

2.2 Sparse reconstruction

Since the InSAR image can be sparsely represented, it becomes a key challenge to reconstruct the image from the echo signal. Compressed sensing is a novel theory focusing on sparse signal compression and reconstruction. N-dimensional signal $\boldsymbol{x}$ is defined K-sparse if it has K or fewer non-zero coordinates:

$$\boldsymbol{x} \in \mathbb{R}^N, \quad \|\boldsymbol{x}\|_0 \stackrel{\text{def}}{=} |\text{supp}(\boldsymbol{x})| \leqslant K \ll N, \tag{4}$$

where we note that $\|\cdot\|_0$ is a quasi-norm [21].

For the sparse signal, CS measures M ($K < M \ll N$) projections of $\boldsymbol{x}$ and reconstructs the sparse signal from this small set of non-adaptive linear measurements. Each measurement can be viewed as an inner product with the signal $\boldsymbol{x} \in \mathbb{R}^N$ and some vector $\boldsymbol{\psi_i} \in \mathbb{R}^N$. If we collect M measurements in this way, we may then consider the $M \times N$ measurement matrix $\boldsymbol{\Psi}$ whose rows are the vectors $\boldsymbol{\psi}_i^{\mathrm{T}}$. Mathematically, a sparsity problem can be described as a problem of finding sparse solutions of a representation or an underdetermined equation, that is, recovering the K-sparse signal $\boldsymbol{x} \in \mathbb{R}^N$ from its measurement vector $\boldsymbol{y} = \boldsymbol{\Psi x} \in \mathbb{R}^M$. The problem then can be modeled as the following ℓ_0-optimization problem:

$$\min_{\boldsymbol{x} \in \mathbb{R}^N} \|\boldsymbol{x}\|_0 \quad \text{s.t.} \quad \boldsymbol{y} = \boldsymbol{\Psi x}. \tag{5}$$

Since $M \ll N$, the sparsity problems are seriously ill-posed and may have multiple solutions. A common practice is then to apply regularization technique for the solutions. Thus, the sparsity problems can be frequently transformed into the following so called ℓ_0-regularization problem:

$$\min_{\boldsymbol{x} \in \mathbb{R}^N} \left\{ \|\boldsymbol{y} - \boldsymbol{\Psi x}\|_2^2 + \xi \|\boldsymbol{x}\|_0 \right\}, \tag{6}$$

where parameter ξ is used to balance the two objective terms. Many researchers have suggested an approximate solution of (5) by relaxing the ℓ_0-norm to ℓ_p-norm ($0 < p \leqslant 1$) or other approach for ℓ_p-norm also promotes sparsity in a solution. Among these approaches, ℓ_1-regularization becomes widespread that many research has studied the property of ℓ_1-regularization and algorithms to solve the ℓ_1-regularization optimization problems. However, for many applications, the solutions of the ℓ_1-regularization are less sparse than those of the ℓ_0-regularization [22]. It may come with the problems such as introducing extra bias in estimation. In this paper, instead of ℓ_1-minimization, we choose a powerful approach $\ell_{1/2}$-minimization ($p = 1/2$) to reconstruct the sparse signal,

$$\min_{\boldsymbol{x} \in \mathbb{R}^N} \left\{ \|\boldsymbol{y} - \boldsymbol{\Psi x}\|_2^2 + \xi \|\boldsymbol{x}\|_{1/2}^{1/2} \right\}, \tag{7}$$

since $\ell_{1/2}$-regularizations may generate more sparse solutions than ℓ_1-regularization and provide a faster computational speed in some cases [23].

3 Data processing method

In the case of an InSAR system, the geometry and data acquisition model are shown in Figure 3. Compared with the conventional InSAR sampling uniformly, the model of this paper transmits and receives pulses randomly in the azimuth direction. Zero azimuth time ($\eta = 0$) is defined at zero Doppler and the

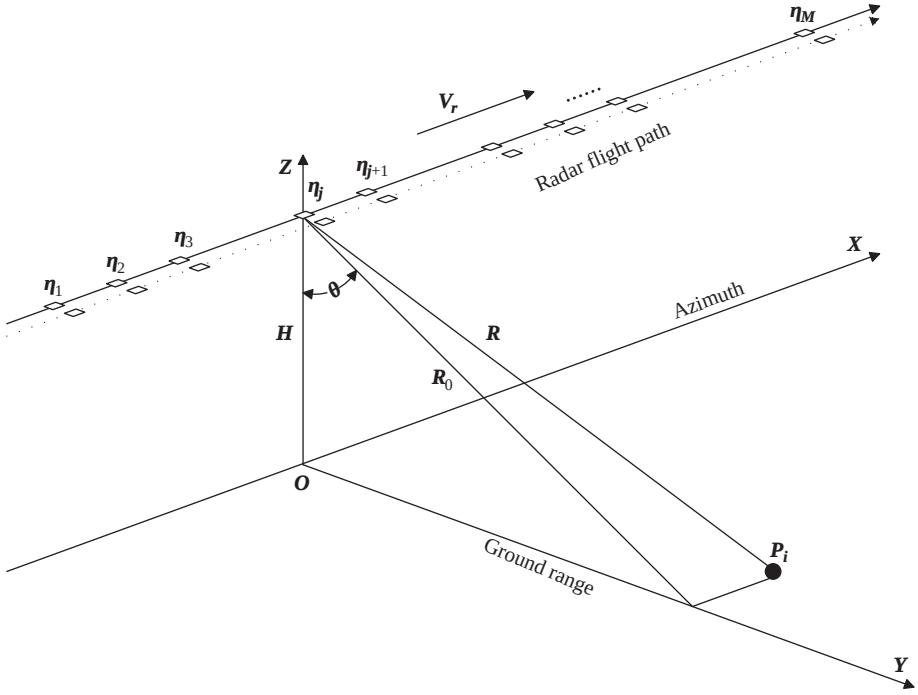

Figure 3 InSAR data acquisition model.

instantaneous slant range $R(\eta)$ from antenna to a single point P_i at a position $(R_0, V_r\eta)$ can be modelled as

$$R(\eta) = \sqrt{R_0^2 + V_r^2\eta^2} \approx R_0 + \frac{V_r^2\eta^2}{2R_0}, \tag{8}$$

where V_r is the platform velocity. After demodulation to baseband, the acquired raw data for P_i whose backscatter coefficient is σ_i can be written in terms of the range time τ and azimuth time η,

$$s(\tau,\eta) = \sigma_i w_{\mathrm{r}}\left[\tau - \frac{2R(\eta)}{\mathrm{c}}\right] w_{\mathrm{a}}(\eta-\eta_{\mathrm{c}}) \exp\left\{\mathrm{j}\pi K_{\mathrm{r}}\left[\tau - \frac{2R(\eta)}{\mathrm{c}}\right]^2\right\} \exp\left[-\mathrm{j}\frac{4\pi f_0 R(\eta)}{\mathrm{c}}\right], \tag{9}$$

where η_{c} is the beam center offset time, f_0 denotes the carrier frequency, K_{r} denotes the chirp rate. $w_{\mathrm{a}}(\cdot)$ is the weighting in azimuth from the antenna pattern, $w_{\mathrm{r}}(\cdot)$ is the range envelope and c is the speed of light.

Use the conventional matcher filter, the output of the range compression can be written as

$$s_{\mathrm{rc}}(\tau,\eta) = \sigma_i p_{\mathrm{r}}\left[\tau - \frac{2R(\eta)}{\mathrm{c}}\right] w_{\mathrm{a}}(\eta-\eta_{\mathrm{c}}) \exp\left[-\mathrm{j}\frac{4\pi f_0 R(\eta)}{\mathrm{c}}\right], \tag{10}$$

where $p_{\mathrm{r}}(\cdot)$ denotes the point spread function of $w_{\mathrm{r}}(\cdot)$.

For simplicity, only low squint angle situation is deduced and some procedures in range-Doppler (RD) algorithm are used in the processing. Hence, the signal of (10) can be approximated as

$$s_{\mathrm{rcmc}}(\tau,\eta) = \sigma_i p_{\mathrm{r}}\left[\tau - \frac{2R(\eta)}{c}\right] w_{\mathrm{a}}(\eta-\eta_{\mathrm{c}}) \exp\left[-\mathrm{j}\frac{4\pi f_0 R_0}{c}\right] \exp\left[-\mathrm{j}\pi\frac{2V_r^2}{\lambda R_0}\eta^2\right]. \tag{11}$$

The range migration delay in (11) is removed during processing by range cell migration correction (RCMC). Assuming a range cell contains K scattering centers with different azimuth locations x_i' in the total illumination time T_0, we have the signal after RCMC in the range cell corresponding to R_0 as follows:

$$s_{\mathrm{rcmc}}(\tau,\eta) = \sum_{i=0}^{K} \sigma_i p_{\mathrm{r}}\left[\tau - \frac{2R_0}{\mathrm{c}}\right] w_{\mathrm{a}}\left(\eta-\eta_{\mathrm{c}}-\frac{x_i'}{V_r}\right) \exp\left[-\mathrm{j}\pi\frac{2V_r^2}{\lambda R_0}\left(\eta-\frac{x_i'}{V_r}\right)^2\right] \cdot \exp\left[-\mathrm{j}\frac{4\pi f_0 R_0}{\mathrm{c}}\right]. \tag{12}$$

The RCMC is achieved by the RD framework and the signal is assumed uncoupled in azimuth and range direction. Then, Eq. (12) is simplified as

$$s(\eta) = \sum_{i=0}^{K} \sigma_i w_{\mathrm{a}} \left(\eta - \eta_{\mathrm{c}} - \frac{x_i'}{V_r}\right) \exp\left[-\mathrm{j}\pi \frac{2V_r^2}{\lambda R_0} \left(\eta - \frac{x_i'}{V_r}\right)^2\right]. \tag{13}$$

Discretize the azimuth time η into $\boldsymbol{\eta} = [\eta_1, \eta_2, \ldots, \eta_M]^{\mathrm{T}}$ ($[\cdot]^{\mathrm{T}}$ denotes vector or matrix transpose) shown in Figure 3 and construct the matrix

$$\boldsymbol{\Phi} = [\boldsymbol{h_1}, \boldsymbol{h_2}, \ldots, \boldsymbol{h_N}], \tag{14}$$

where

$$\boldsymbol{h_i} = w_{\mathrm{a}} \left(\boldsymbol{\eta} - \eta_{\mathrm{c}} - \frac{x_i}{V_r}\right) \exp\left[-\mathrm{j}\pi \frac{2V_r^2}{\lambda R_0} \left(\boldsymbol{\eta} - \frac{x_i}{V_r}\right)^2\right], \tag{15}$$

where $x_i = (i - 1 - N/2)\Delta x$ $(i = 1, 2, \ldots, N)$ is the ith azimuth location in the illuminated area. The azimuth sampling interval Δx is related to the azimuth resolution. In general, Δx can be set equal to or a little less than V_r/PRF and set N an even number greater than $V_r T_0/\Delta x$. Considering the noise $\boldsymbol{n}$, the echo signal can be expressed as

$$\boldsymbol{s}_{M\times 1} = \boldsymbol{\Phi}_{M\times N} \boldsymbol{\sigma}_{N\times 1} + \boldsymbol{n}_{N\times 1}, \tag{16}$$

where $\boldsymbol{\sigma}$ is the complex-valued image of the range cell R_0 with N elements σ_i and $\boldsymbol{s} = s(\boldsymbol{\eta})$ is the discrete echo with M elements. It is worth noting that although Eq. (16) is conducted when the squint angle is low, the model can be applied to large RCM cases. In such cases, one-dimensional processing becomes a two-dimensional problem and the subscripts in (16) should be modified considering the range cell numbers. As aforementioned, the complex-valued SAR image has less sparsity and can hardly be sparsely represented under common sparse frameworks.

However, inspired by the idea in (3), the complex-valued image $\boldsymbol{\sigma}$ in (16) can be sparsely represented by cancelling $\boldsymbol{\phi}'$, the phase of the image acquired by antenna A_2 corresponding to the same range cell R_0. Therefore, each image element of antenna A_1 can be rewritten as $\sigma_i = \sigma_i' \exp(\mathrm{j}\phi_i')$ and the signal can be modeled as

$$\boldsymbol{s} = \boldsymbol{\Phi P \sigma}_{\mathrm{new}} + \boldsymbol{n}, \tag{17}$$

where the matrix $\boldsymbol{P} = \mathrm{diag}\{\exp(\mathrm{j}\phi_i')\}$ is a diagonal matrix where ϕ_i' denotes the ith elements of $\boldsymbol{\phi}'$ and $\boldsymbol{\sigma}_{\mathrm{new}}$ is the new reconstructed complex-valued image with N elements σ_i'. The new image $\boldsymbol{\sigma}_{\mathrm{new}}$ combining the magnitude information of image $\boldsymbol{\sigma}$ and the interferometric phase can be sparsely represented. Thus, we consider

$$\boldsymbol{\sigma}_{\mathrm{new}} = \boldsymbol{\Psi \alpha}, \tag{18}$$

where $\boldsymbol{\Psi}$ is an appropriate dictionary for the model that represents the new image sparsely and $\boldsymbol{\alpha}$ is the coefficient under dictionary $\boldsymbol{\Psi}$. Substitute (18) into (17), the imaging model can be rewritten as

$$\boldsymbol{s} = \boldsymbol{\Phi P \Psi \alpha} + \boldsymbol{n}. \tag{19}$$

If the phase matrix $\boldsymbol{P}$ is known, the problem turns into a typical sparse reconstruction problem:

$$\hat{\boldsymbol{\alpha}} = \arg\min_{\boldsymbol{\alpha}} \{\|\boldsymbol{s} - \boldsymbol{\Phi P \Psi \alpha}\|_2^2 + \lambda \|\boldsymbol{\alpha}\|_p\}. \tag{20}$$

Unfortunately, the phase term matrix $\boldsymbol{P}$ of the antenna A_2 is unknown due to the sparse sampling. Here we use the conventional imaging method to form the image of the antenna A_2. The imaging result may suffer from high sidelobes, but has a strong correlation with the image formed by all samples. Hence, we can substitute the phase of this image for the phase term matrix in (20). Using the substitution, the optimization problem becomes

$$\hat{\boldsymbol{\alpha}} = \arg\min_{\boldsymbol{\alpha}} \{\|\boldsymbol{s} - \boldsymbol{\Phi P' \Psi \alpha}\|_2^2 + \lambda \|\boldsymbol{\alpha}\|_p\}, \tag{21}$$

where $\boldsymbol{P}'$ is the phase term matrix of the image formation by the conventional imaging approaches. Quite a number of algorithms have been proposed and studied for solving the problems (20) based on ℓ_1-minimization techniques such as the iterative shrinkage thresholding (IST) method [24]. However, to solve (20) faster and more accurate, we use the iterative half thresholding technique based on $\ell_{1/2}$-minimization to get $\hat{\boldsymbol{\alpha}}$ [22].

Noticed that Eq. (21) is a complex-valued optimization problem, when $\ell_{1/2}$-minimization is applied, an extension of the half thresholding theory established on the complex space is used and the solutions of problem (21) can be expressed by

$$\boldsymbol{\alpha} = G_{\lambda\mu,1/2}\left(\boldsymbol{\alpha} + \mu \boldsymbol{A}^{\mathrm{H}}\left(\boldsymbol{s} - \boldsymbol{A}\boldsymbol{\alpha}\right)\right), \tag{22}$$

where $\boldsymbol{A} = \boldsymbol{\Phi}\boldsymbol{P}'\boldsymbol{\Psi}$, μ is the a step size and $G_{\lambda\mu,1/2}(\cdot)$ is the complex-valued half thresholding function defined in [25]. More details about the complex-valued half thresholding algorithm can be seen in [25,26]. With the iteration representation (22), the new complex-valued image which contains the magnitude and inteferogram phase information of the scene can be acquired by inverse transformation $\hat{\boldsymbol{\sigma}}_{\mathrm{new}} = \boldsymbol{\Psi}\hat{\boldsymbol{\alpha}}$.

4 Experiments and results

This section presents some results obtained by processing simulated and real data to show the effectiveness of the proposed method.

4.1 Experiments description

For sparse sampling, we choose M-sequence to sample in the azimuth direction with "1" in the sequence represents the sampling position and "0" the vacant position.

M-sequence, or maximum length sequence (MLS) is binary sequence generators that are capable of outputting all possible combinations of binary sequences in $2^n - 1$ cyclic shifts, where n is the size of the linear feedback shift registers used in generating such sequences[1)].

M-sequences are inexpensive to implement in hardware or software, and relatively low-order feedback shift registers can generate long sequences; a sequence generated using a shift register of length 20 is $2^{20} - 1$ samples long.

Another reason we choose M-sequence is its good autocorrelation properties (a single peak with no sidelobes) which simplify the recovery process. An M-sequence can be shown to have a thumbtack-like autocorrelation function [27]. Therefore, terms like psuedorandom binary sequences or psuedonoise sequences are also used to refer M-sequences. Figure 4 shows the autocorrelation function (ACF) of a M-sequence with $n = 10$ and length $p = 2^{10} - 1 = 1023$. As seen in Figure 4, the M-sequence has a certain degree of randomness which contributes to the reconstruction. M-sequence is irrelevant with the sparsity of the scene, which means it can be used repetitively and the hardware cost can be reduced in the practical cases.

An M-sequence has 2^{n-1} "1"s and $2^{n-1} - 1$ "0"s, the occurrence of 0 and 1 in the sequence is approximately the same, so the sparse rate of the data acquisition is about 50% in the experiments.

For the sparse representation, Fourier transform is chosen to represent the image in the experiment. Fourier basis is a simple and popular dictionary. Figure 2 has shown that under Fourier basis, the new image $\boldsymbol{\sigma}_{\mathrm{new}}$ can be sparsely represented. In the practical cases, the other bases can be used according to the scene. A rough imaging can be done to get the prior information of the scene and the corresponding sparse basis can be chosen. CS theory points out that it has to satisfy an incoherency property between $\boldsymbol{\Phi}\boldsymbol{P}'$ and $\boldsymbol{\Psi}$ to recover the signal. It needs $\boldsymbol{\Phi}\boldsymbol{P}'$ to be incoherent in the $\boldsymbol{\Psi}$ domain. To evaluate the incoherence, mutual coherence defined by

$$\mu(B, C) = \max_{k,j} \frac{|\langle b_k, c_j\rangle|}{\|b_k\|_2 \|c_j\|_2} \tag{23}$$

1) Maximum length pn sequence generation. http://www.mathworks.de/matlabcentral/linkexchange/links/2324-maximum-length-pn-sequence-generation.

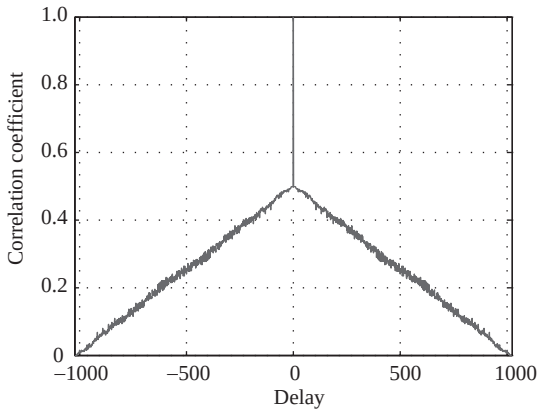

Figure 4 The autocorrelation function of an M-sequence.

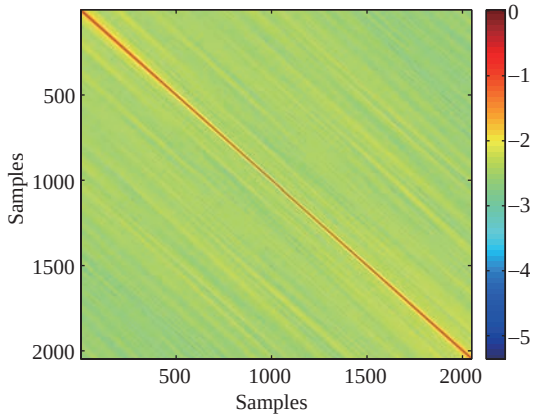

Figure 5 Coherence matirx of $\boldsymbol{A}$.

is used. The parameter $\mu(B,C)$ serves as a rough characterization of the degree of similarity between matrices B and C, where b_k is the kth row of the matrix B and c_j is the jth column of the matrix C [28]. In our case, $\boldsymbol{\Psi}$ is the inverse Fourier transform matrix, with the chosen step, $\mu(\boldsymbol{\Phi P}', \boldsymbol{\Psi})$ attains a value about 0.12 (minimum value $1/\sqrt{N} = 0.03$).

With the chosen matrix and sparse representation, each column of $\boldsymbol{A}$ is highly incoherent, Figure 5 shows the logarithmic autocorrelation matrix of rows from $\boldsymbol{A}$. The matrix is close to an identity matrix, which indicates that $\boldsymbol{A}$ approximately satisfies the orthogonality and can be used to recover the signal.

The InSAR images after cancelling the common backscatter phase are also sparse in other transform domains and dictionaries such as wavelets basis can be used to sparsely represent the complex-valued InSAR images. Ref. [29] studied the sparse regularization of interferometric phase and amplitude for InSAR image formation from Bayesian perspective and such studies worth deeper researching.

For the computational complexity, it can be analyzed according to (22). For each range cell, the computational complexity of $\mu \boldsymbol{A}^{\mathrm{H}}(\boldsymbol{s} - \boldsymbol{A\alpha})$ is $\mathcal{O}(MN)$ and the half thresholding operator take $\mathcal{O}(N)$ in each iteration. Hence, the total computational complexity of an iteration is $\mathcal{O}(MN)$, which is the same order with that of the soft algorithm. The convergence speed is analyzed in [30], the number of iteration requires of the proposed method are nearly the same with some ℓ_1 based algorithm. Therefore, the total time consuming of the proposed method is the same with those ℓ_1 based algorithm. To shorten the time consuming, some accelerated $\ell_{1/2}$ regularization algorithms such as the method proposed in [26] can be applied. However, the conventional match filter method only involves some matrix multiplication and fast Fourier Transform (FFT) operation. The computational complexity is $\mathcal{O}(N \log N)$. The cost is much higher compared to conventional method which would entail a new study about fast $\ell_{1/2}$ regularization techniques.

4.2 Evaluation principle

To provide a numerical evaluation for the results, we consider images that directly use the ground truth. First idea for evaluation could be the complex correlation function γ [2], which is widely used in the interferometry and is defined as

$$\gamma = \frac{E[\hat{\boldsymbol{v}}\boldsymbol{v}^*]}{\sqrt{E[\hat{\boldsymbol{v}}\hat{\boldsymbol{v}}^*]E[\boldsymbol{v}\boldsymbol{v}^*]}}, \tag{24}$$

where $\hat{\boldsymbol{v}}$ represents the imaging results acquired by the specified method, $\boldsymbol{v}$ represents the ground truth image, $(\cdot)^*$ denotes the complex conjugate and $E[\cdot]$ denotes averaging over the ensemble of image realizations. An estimate of coherence can be obtained through spatial averaging. The correlation function is used to judge the relationship between the scattered fields at the interferometric receivers after image formation, while we use γ here to judge the relationship between imaging results and the ground truth and evaluate the image quality. For completely coherent image results, we have $\gamma = 1$, while $\gamma = 0$ when

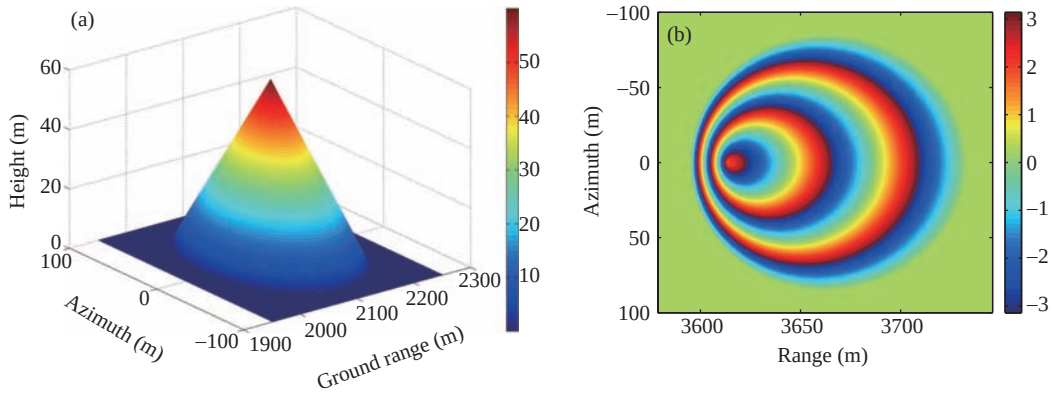

Figure 6 Simulated scene. (a) DEM; (b) ideal interferometric phase.

the image results are independent, which indicates the imaging results are far from the truth and the specified method malfunctions.

Another idea to evaluate the reconstructed image is the mean squared error (MSE) which also indicates the SNR of the image. MSE can be defined as [17]

$$\mathrm{MSE} = \frac{1}{N}\||\boldsymbol{v}| - |\hat{\boldsymbol{v}}|\|_2^2, \tag{25}$$

where $|\boldsymbol{v}|$ and $|\hat{\boldsymbol{v}}|$ are the true and reconstructed magnitude images and N is the number of resolution elements in the reconstructed image.

Since our result is a complex-valued image and the image phase contains the interferogram information, an evaluation for phase is necessary. Here we use mean phase error (MPE) which can be expressed as

$$\mathrm{MPE} = \frac{1}{N}\|\angle\boldsymbol{v} - \angle\hat{\boldsymbol{v}}\|_1, \tag{26}$$

where $\angle\boldsymbol{v}$ is the phase of the ground truth and $\angle\hat{\boldsymbol{v}}$ denotes reconstructed phase.

4.3 Simulated data

To analyze the effects due to the reduced number of acquisitions and to their non-uniform spacing, and to show phase-preserving capabilities of the proposed method, we perform some experiments on simulated data. For comparison, the conventional interferometry [31], including imaging, precise image registration, interferogram generation and filtering and other procedures is also performed here.

Figure 6(a) shows the simulated scene. To avoid the sparse scene such as point-target, we consider a scene which contains a cone with 60 meters high and a radius of 120 meters on the ground for simulation. The whole scene is 200 m $\times$ 300 m in the azimuth-ground range plane. The backscatter coefficients of the cone is 1 and the ground is 0.3. Considering the backscatter random phase, a white zero-mean Gaussian noise is multiplied during the raw data generation. The synthetic aperture time is about 1 s and 2048 pulses are used to reconstruct the scene. The detailed simulation parameters are listed in Table 1.

To prove the feasibility of the substitution in (21), a comparison between sparse sampling and full sampling imaging results is made here. Here we use 1024 pulses (50%) and 683 pulses (33%) of azimuth sparse sampling to form the image, respectively. 500 Monte Carlo trials are conducted for each azimuth sampling number. When the simulated scene imaging is formed using half of the samplings, the average MPE is 4.14°. When the sampling number falls down to 683, the average MPE of 500 trials is 5.95°. The sparse sampling imaging result will suffer phase loss, however, it can be used for substitution in (21) since the phase loss is small.

The ideal interferometric phase of the ground truth is shown in Figure 6(b). The phases here are the principal value, modulo 2π, from $-\pi$ (blue) to π (red). To make the illustration more intuitive and the comparison more accurate, the flat earth phase contribution is removed before display and evaluation.

Table 1 Simulation parameters

Parameter	Notation	Value
Carrier frequency	f_c	35 GHz
Incidence angle	θ	35°
Baseline	B	1 m
Platform height	H	3000 m
Platform velocity	V_r	50 m/s
Pulse repetition frequency	PRF	200 Hz
Range sampling rate	f_s	600 MHz
System bandwidth	B_s	400 MHz
Antenna size	D	0.6 m

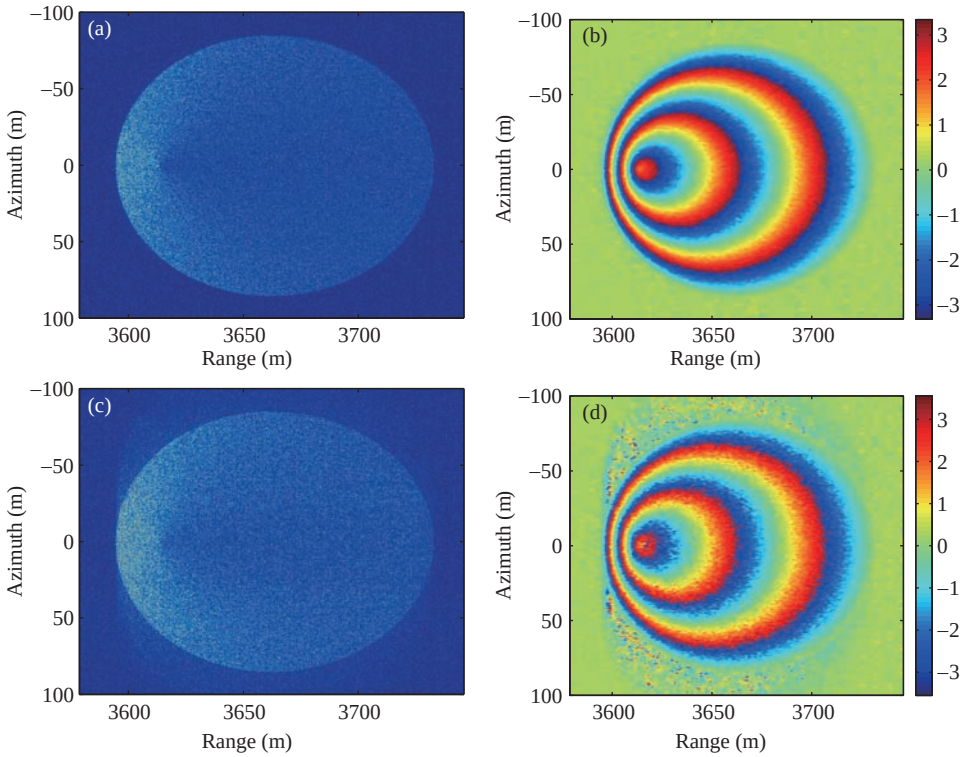

Figure 7 RDA results (noise free). (a) Magnitude (all samples); (b) interferometric phase (all samples); (c) magnitude (50% samples); (d) interferometric phase (50% samples).

Figure 7 shows the RDA imaging results which we use here to compare the performances of the proposed method. Figure 8 is the imaging results of the proposed method with all samples and 50% samples without noise. To show the capabilities of the proposed method under different noise conditions, an additive Gaussian white noise is added in the simulated raw echo to generate different noise levels (single pulse SNR = 0 dB, −10 dB) and Figures 9 and 10 show the interferometric imaging results of different approaches in the case single pulse SNR = −10 dB.

The evaluation results are given in Table 2. Here the image coherence is evaluated separately which γ_{abs} and γ_{phase} denote the coherence of the image magnitude and phase, respectively. To depress the noise impact on the image, pivoting median filter [32] is used and different sizes of windows are tried to smooth the image. In Table 2, the subscript 1 means imaging using the proposed method with all samples and 2 means using 50% of the samples. It is observed that by using all the samples, the imaging results of the proposed method are the same as the performance of the conventional interferometry techniques. When the number of samples decreases, the results show that the image quality of both the methods degrades. However, the proposed method can still obtain the magnitude image and interferometric phase

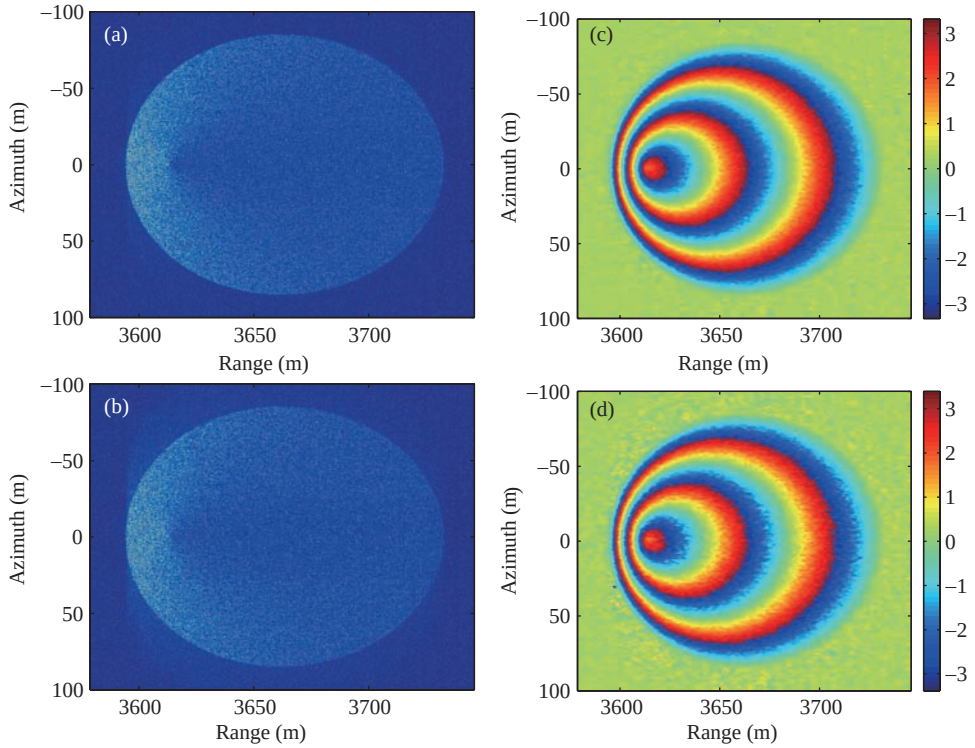

Figure 8 CS results (noise free). (a) Magnitude (all samples); (b) interferometric phase (all samples); (c) magnitude (50% samples); (d) interferometric phase (50% samples).

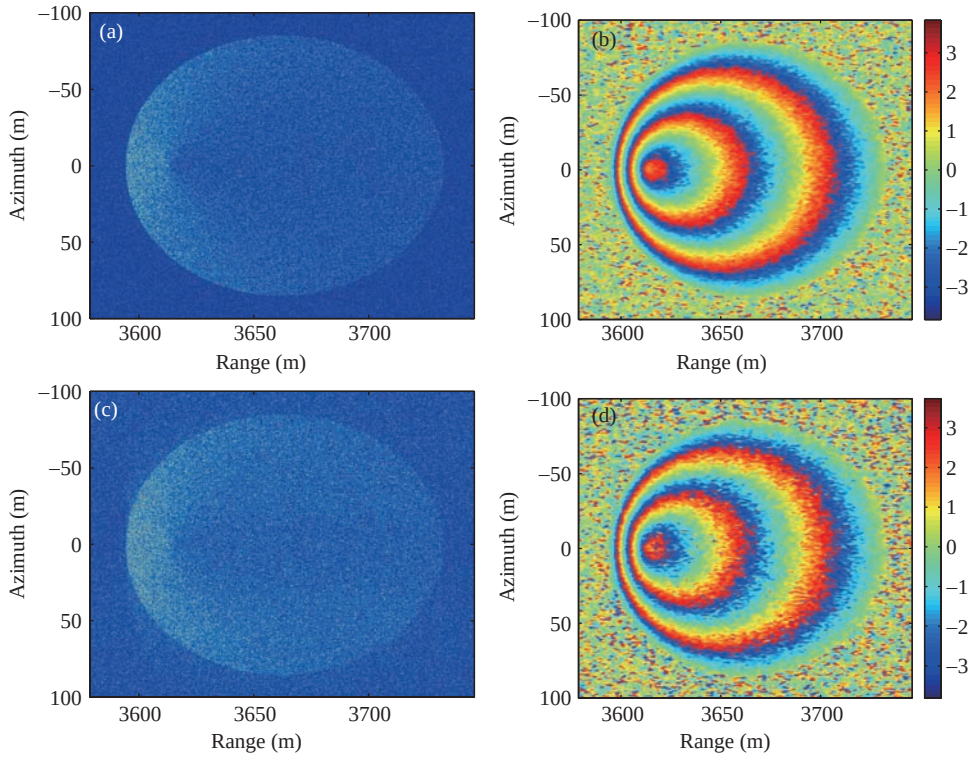

Figure 9 RDA results (SNR = −10 dB). (a) Magnitude (all samples); (b) interferometric phase (all samples); (c) magnitude (50% samples); (d) interferometric phase (50% samples).

within the tolerance error in high SNR condition while the conventional interferometry approach suffers great from high sidelobes. (When MPE = 10°, the corresponding height measurement error is 0.94 m.

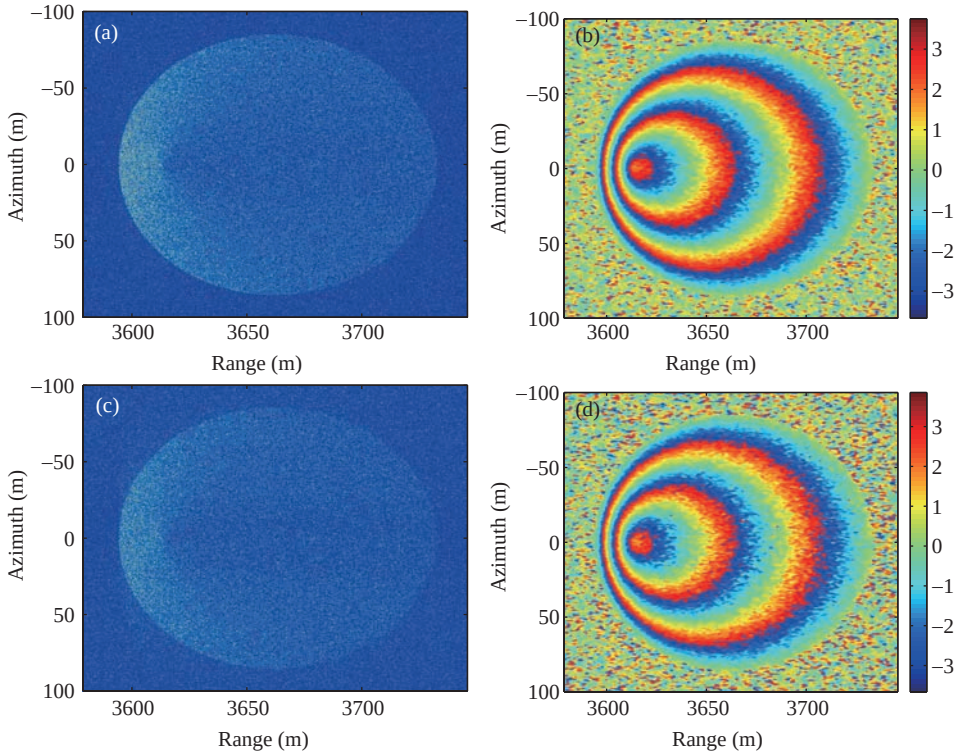

Figure 10 CS results (SNR = −10 dB). (a) Magnitude (all samples); (b) interferometric phase (all samples); (c) magnitude (50% samples); (d) interferometric phase (50% samples).

Since our InSAR system height measurement accuracy is 0.99 m, the error is tolerable in some case such as emergency mapping.) The CS method preserves the image phase and performs better when using less acquisition samples.

4.4 Real data

We present the experiments on real data in the following part. In particular, we consider the agriculture area in Xi'an, China. The scatterers distribute uniformly in the illuminated area and the sparse assumption that the most papers studied is not suitable.

The InSAR flight experiment was operated on May 16, 2011. In the experiment, the aeroplane flew at about 3000 m high with the velocity of 47.9 m/s and the system PRF is 1000 Hz. The ground altitude is about 300 m. We use antennas 1 and 2 for imaging whose baseline length is 0.6 m. The time width of chirp signal is 12 μs. Other parameters are listed in Table 1. The InSAR system operated on standard mode that only antenna 1 transmitted the chirp signal and both antennas received the echoed signal.

Before the proposed method implementation, the errors arising from the aircraft movements are compensated by a two step motion compensation during the SAR imaging processing [33, 34]. Additionally, a very precise velocity and range delay variation compensation has been carried out.

The image formation results of different approaches are listed below. Figure 11 is the imaging results using chirp scaling algorithm (CSA) and the conventional SAR interferometry flow where (a) is the image magnitude and (b) is the image phase. Figure 12 shows the imaging results using the proposed method with full samples (2048 samples) and Figure 13 uses half of the samples. We show the coherence images of imaging phase in Figure 12(c) and Figure 13(c) where we can see that the image phase of the proposed method is highly coherent with the results of the conventional approach.

It is a pity that we do not have the ground truth or higher precision data for the experiments with the real data. However, we still make a comparison with the conventional InSAR results to set an approximate evaluation on the proposed method. The evaluation results are given in Table 3. As seen in the table, the proposed method performs nearly the same using the full samples. When using 50% samples, the image

Table 2 Simulation evaluation

	Window	MSE	MPE	γ_{abs}	γ_{phase}
			Noise free		
RD_1	5×5	0.4033	7.7318	0.9435	0.9885
RD_2	5×5	0.4246	16.1688	0.9405	0.8993
CS_1	5×5	0.3895	7.5999	0.9441	0.9834
CS_2	5×5	0.4117	11.8588	0.9428	0.9542
RD_1	7×7	0.3464	7.6803	0.9516	0.9878
RD_2	7×7	0.3795	13.6570	0.9495	0.9278
CS_1	7×7	0.3440	7.0813	0.9518	0.9875
CS_2	7×7	0.3714	9.6770	0.9503	0.9698
			SNR = 0		
RD_1	5×5	0.4297	11.0752	0.9415	0.9839
RD_2	5×5	0.4639	20.0382	0.9387	0.8951
CS_1	5×5	0.4369	11.0750	0.9435	0.9831
CS_2	5×5	0.4455	15.4450	0.9409	0.9438
RD_1	7×7	0.4011	9.9295	0.9513	0.9871
RD_2	7×7	0.4258	16.2879	0.9498	0.9234
CS_1	7×7	0.4100	9.2649	0.9513	0.9842
CS_2	7×7	0.4155	12.7845	0.9503	0.9628
			SNR = −10 dB		
RD_1	5×5	0.4449	23.1369	0.9359	0.9421
RD_2	5×5	0.4755	37.9985	0.9140	0.7699
CS_1	5×5	0.4350	23.1223	0.9358	0.9425
CS_2	5×5	0.4739	30.4115	0.9211	0.8413
RD_1	7×7	0.4235	19.3985	0.9422	0.9472
RD_2	7×7	0.4283	31.9880	0.9216	0.8096
CS_1	7×7	0.4149	19.2339	0.9422	0.9495
CS_2	7×7	0.4639	26.5798	0.9283	0.8667

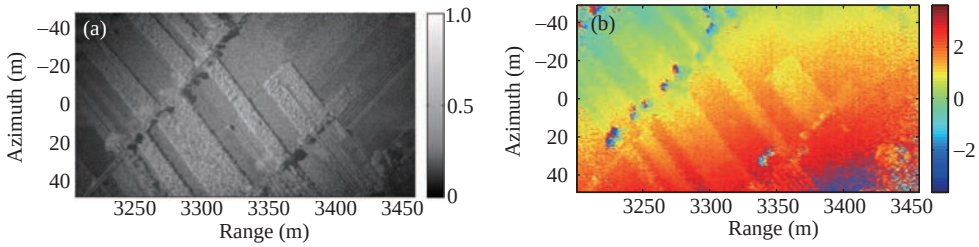

Figure 11 Chirp scaling results. (a) Magnitude; (b) interferometric phase.

quality only deteriorates a little which can be tolerable in practice. The interferogram can be further used in digital elevation model (DEM) generation.

5 Conclusion and future developments

This paper presents a CS-based InSAR imaging approach which allows the scene reconstruction using sparsely sampled data acquisition. The method exploits the information of two antennas to cancel the common backscatter random phase of the same resolution element, so that a sparse representation for the InSAR images can be used. The proposed method reduces the restriction and extends the CS application in SAR imaging. The main feature of the proposed method is allowing a reduction of the number of acquisitions required for InSAR image formation with respect to conventional interferometry methods. The data acquisition can be non-uniformly sampled in the real system and data volume is decreased

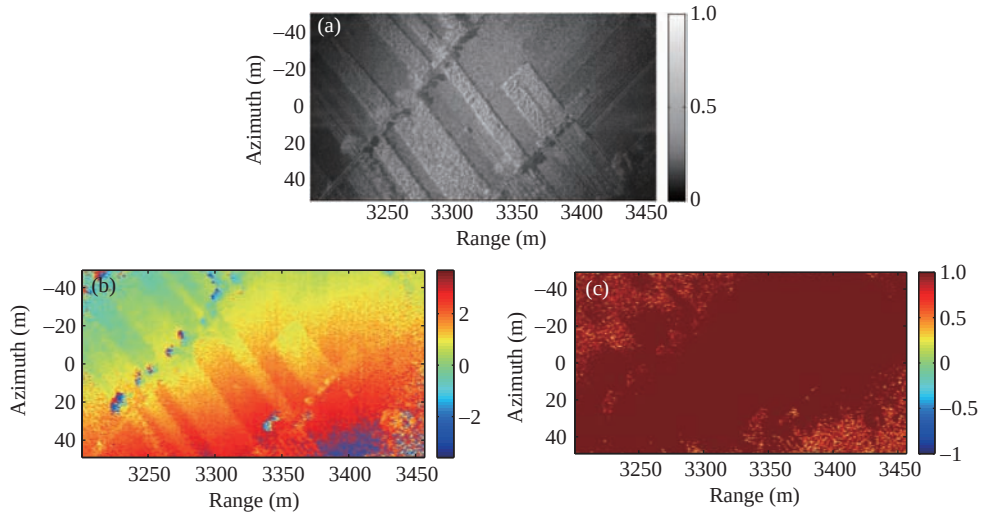

Figure 12 Compressed sensing results (full samples). (a) Magnitude; (b) interferometric phase; (c) coherent coefficient.

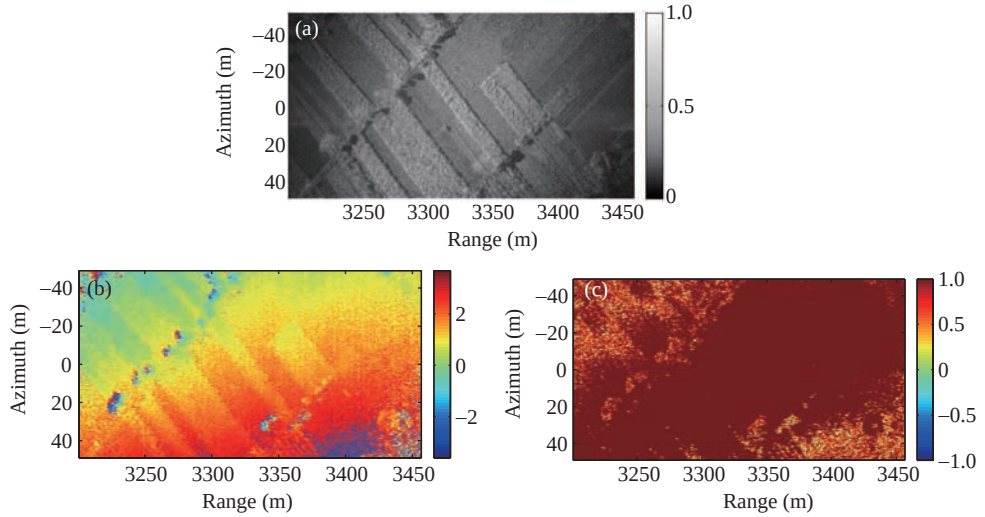

Figure 13 Compressed sensing results (50% samples). (a) Magnitude; (b) interferometric phase; (c) coherent coefficient.

Table 3 Real data results evaluation

	MSE	MPE	γ_{abs}	γ_{phase}
CS_1	0.0345	3.6981	0.9872	0.9501
CS_2	0.0392	9.2247	0.9534	0.9019

which will release great pressure on transmission and storage. The main contribution of this paper is that we proposed a method complex-valued SAR images can be sparsely represented by uniting the data from different channels.

Experiment results on simulated data show that image quality obtained by the CS-based method performs better than that obtained using conventional interferometry methods when the acquired data decreased. The proposed method can preserve the interferometric phase better than the conventional method under the same noise level. In high SNR condition, the imaging results which contain the information of both magnitude and interferometric phase can be further developed in DEM generation and InSAR applications. This property has also been confirmed from the three-baseline millimeter wave InSAR experiments data.

To develop the potentialities of the proposed method, a further research would be required. The current work still needs to get the image of antenna A_2 using conventional imaging method and does not

combine the multi-channel data completely. The full combination of the data from different antennas would gain more information and enhance the image quality. For sparse representation, Fourier basis is used in this paper. However, to deal with a more complicated scene, Fourier basis may deteriorate and an appropriate basis would substitute. For example, Haar wavelets can be used to represent the image with many sharp edges. If the complex-valued SAR image can be represented more sparsely, it may use less sampling to get the InSAR image. With the change of the sparse basis, the sampling method may also need adjustment. Instead of M-sequence, a more sparse sampling sequence can be developed. Since our work focuses on processing sparse data acquisitions, both issues and their relationships are worthy of a deep research. Moreover, we only discuss the CS application in cross-track interferometry in this paper while the proposed method may extend to other InSAR modes. Since the preliminary experiments in this paper show very positive results, these issues look very promising.

Acknowledgements This work was supported by National Natural Science Foundation of China (Grant No. 61271422).

Conflict of interest The authors declare that they have no conflict of interest.

References

1 Graham L C. Synthetic interferometer radar for topographic mapping. Proc IEEE, 1974, 62: 763–768
2 Bamler R, Hartl P. Synthetic aperture radar interferometry. Inverse Problem, 1998, 14: 1–54
3 Allen C T. Interferometric synthetic aperture radar. IEEE Geosci Remote Sens Soc Newslett, 1995, 96: 6–13
4 Berardino P, Fornaro G, Lanari R, et al. A new algorithm for surface deformation monitoring based on small baseline differential sar interferograms. IEEE Trans Geosci Remote Sens, 2002, 40: 2375–2383
5 Donoho D L. Compressed sensing. IEEE Trans Inf Theory, 2006, 52: 1289–1306
6 Candes E J, Romberg J, Tao T. Robust uncertainty principles: exact signal reconstruction from highly incomplete frequency information. IEEE Trans Inf Theory, 2006, 52: 489–509
7 Baraniuk R, Steeghs P. Compressive radar imaging. In: Prcoeedings of IEEE Radar Conference, Boston, 2007. 128–133
8 Zhang L, Xing M D, Qiu C W, et al. Achieving higher resolution isar imaging with limited pulses via compressed sampling. IEEE Geosci Remote Sens Lett, 2009, 6: 567–571
9 Schmitt M, Stilla U. Compressive sensing based layover separation in airborne single-pass multi-baseline InSAR data. IEEE Geosci Remote Sens Lett, 2013, 10: 313–317
10 Budillon A, Evangelista A, Schirinzi G. Three-dimensional sar focusing from multipass signals using compressive sampling. IEEE Trans Geosci Remote Sens, 2011, 49: 488–499
11 Fornaro G, Lombardini F, Pauciullo A, et al. Tomographic processing of interferometric sar data: developments, applications, and future research perspectives. IEEE Signal Process Mag, 2014, 31: 41–50
12 Zhu X X, Bamler R. Superresolving sar tomography for multidimensional imaging of urban areas: compressive sensing-based tomosar inversion. IEEE Signal Process Mag, 2014, 31: 51–58
13 Li J, Xing M D, Wu S. Application of compressed sensing in sparse aperture imaging of radar. In: Proceedings of the 2nd Asian-Pacific Conference on Synthetic Aperture Radar, Xi'an, 2009. 651–655
14 Austin C D, Ertin E, Moses R. Sparse signal methods for 3-D radar imaging. IEEE J Sele Topics Signal Process, 2011, 5: 408–423
15 Potter L C, Ertin E, Parker J T, et al. Sparsity and compressed sensing in radar imaging. Proc IEEE, 2010, 98: 1006–1020
16 Hou X, Yang J, Jiang G, et al. Complex sar image compression based on directional lifting wavelet transform with high clustering capability. IEEE Trans Geosci Remote Sens, 2013, 51: 527–538
17 Samadi S, Cetin M, Masnadi-Shirazi M A. Sparse representation-based synthetic aperture radar imaging. IET Radar Sonar Nav, 2011, 5: 182–193
18 Samadi S, Cetin M, Masnadi-Shirazi M A. Sparse signal representation for complex-valued imaging. In: Proceedings of IEEE 13th Digital Signal Processing Workshop and the 5th IEEE Signal Processing Education Workshop, Marco Island, 2009. 365–370
19 Ramakrishnan N, Ertin E, Moses R. Enhancement of coupled multichannel images using sparsity constraints. IEEE Trans Image Process, 2010, 19: 2115–2126
20 Rosen P A, Hensley S, Joughin I R, et al. Synthetic aperture radar interferometry. Proc IEEE, 2000, 88: 333–382
21 Needell D, Vershynin R. Uniform uncertainty principle and signal recovery via regularized orthogonal matching pursuit. Found Comput Math, 2009, 9: 317–334
22 Xu Z B, Zhang H, Wang Y, et al. $L_{1/2}$ regularization. Sci China Inf Sci, 2010, 53: 1159–1169
23 Zeng J, Xu Z, Jiang H, et al. SAR imaging from compressed measurements based on $L_{1/2}$ regularization. In: Proceedings of IEEE International Geoscience and Remote Sensing Symposium (IGARSS), Vancouver, 2011. 625–628

24 Bioucas-Dias J M, Figueiredo M A T. A new twist: two-step iterative shrinkage/thresholding algorithms for image restoration. IEEE Trans Image process, 2007, 16: 2992–3004

25 Zeng J, Xu Z, Zhang B, et al. Accelerated regularization based sar imaging via bcr and reduced newton skills. Signal Process, 2013, 93: 1831–1844

26 Zeng J S, Fang J, Xu Z B. Sparse sar imaging based on $L_{1/2}$ regularization. Sci China Inf Sci, 2012, 55: 1755–1775

27 Cohn M, Lempel A. On fast M-sequence transforms. IEEE Trans Inf Theory, 1977, 23: 135–137

28 Candes E, Romberg J. Sparsity and incoherence in compressive sampling. Inverse Problem, 2007, 23: 969–985

29 Xu G, Xing M D, Xia X G, et al. Sparse regularization of interferometric phase and amplitude for insar image formation based on bayesian representation. IEEE Trans Geosci Remote Sens, 2015, 53: 2123–2136

30 Zeng J, Lin S, Wang Y, et al. $L_{1/2}$ regularization: convergence of iterative half thresholding algorithm. IEEE Trans Signal Process, 2014, 62: 2317–2329

31 Costantini M, Iodice A, Magnapane L, et al. Monitoring terrain movements by means of sparse SAR differential interferometric measurements. In: Proceedings of IEEE 2000 International Geoscience and Remote Sensing Symposium, Honolulu, 2000. 3225–3227

32 Meng D, Sethu V, Ambikairajah E, et al. A novel technique for noise reduction in insar images. IEEE Geosci Remote Sens Lett, 2007, 4: 226–230

33 Stevens D, Cumming I G, Gray A. Options for airborne interferometric sar motion compensation. IEEE Trans Geosci Remote Sens, 1995, 33: 409–420

34 Moreira A, Mittermayer J, Scheiber R. Extended chirp scaling algorithm for air- and spaceborne sar data processing in stripmap and scansar imaging modes. IEEE Trans Geosci Remote Sens, 1996, 34: 1123–1136